THE JOURNAL OF PHYSICAL CHEMISTRY C

pubs.acs.org/JPCC Article

Core–Satellite Gold Nanoparticle Complexes Grown by Inert Gas-Phase Condensation

Junlei Zhao,* Alvaro Mayoral, Lidia Martínez, Mikael P. Johansson, Flyura Djurabekova,* and Yves Huttel*

Cite This: J. Phys. Chem. C 2020, 124, 24441–24450

Read Online

ACCESS | Metrics & More | Article Recommendations | Supporting Information

ABSTRACT: Spontaneous growth of complexes consisted of a number of individual nanoparticles in a controlled manner, particularly in demanding environments of gas-phase synthesis, is a fascinating opportunity for numerous potential applications. Here, we report the formation of such core–satellite gold nanoparticle structures grown by magnetron sputtering inert gas condensation. Combining high-resolution scanning transmission electron microscopy and computational simulations, we reveal the adhesive and screening role of H_2O molecules in formation of stable complexes consisted of one nanoparticle surrounded by smaller satellites. A single layer of H_2O molecules, condensed between large and small gold nanoparticles, stabilizes positioning of nanoparticles with respect to one another during milliseconds of the synthesis time. The lack of isolated small gold nanoparticles on the substrate is explained by Brownian motion that is significantly broader for small-size particles. It is inferred that H_2O as an admixture in the inert gas condensation opens up possibilities of controlling the final configuration of the different noble metal nanoparticles.

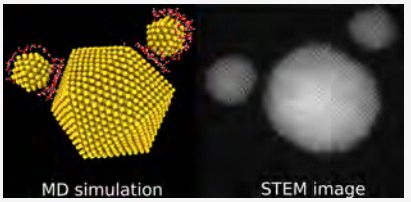

INTRODUCTION

Nanoparticles (NPs) are primary functional building blocks in various fields of nanoscience and nanotechnology, such as gas sensing,[1,2] plasmonics,[3] and surface catalysis.[4,5] Manufacturing NP complexes expands the functionality of nanoscale materials further. In chemical synthesis methods, for example, NP superlattice can be fabricated by controlling preset surface adhesives in liquid phase,[6−8] which is also known as self-assembly. The self-assembly typically relies on the processes driving the system to thermodynamic equilibrium, reaching eventually the stable free-energy minimum of the system.[9−12] However, some metastable configurations can be assembled transiently during the kinetic growth process but are not seen in the final output due to the much shorter lifetime compared with the observational time scale.

Amongst the gas-phase methods available to date, magnetron sputtering inert gas condensation is one of the most flexible and versatile methods[13−27] due to its independence of chemical precursors and surfactants. In particular, the duration of the synthesis process in this unique method does not last longer than a fraction of a millisecond. Therefore, some metastable configurations with the lifetime of micro- or millisecond can be obtained and deposited on a substrate. Despite extensive experience over the past decade of controllable kinetic formation path of individual NPs,[21−23,28−30] complex multi-NPs structures are extremely difficult to architecture within a gas-phase single-step synthesis. The final deposited positions of NPs cannot be determined kinetically by preset growth conditions since the NPs are fabricated via gas-phase condensation in a so-called aggregation zone.[19,27,31] The grown NPs are transferred aerodynamically to the deposition zone, where the final configuration of NPs and positioning on a substrate is randomized by the carrier gas flow.

Conventionally, the condensation process in the magnetron sputtering inert gas condensation chamber involves the high ($\lesssim 10^{-3}$ mbar) and ultrahigh ($\lesssim 10^{-7}$ mbar) vacuum condition. Pure argon and helium are injected into the condensation chamber to induce the sputtering of the target material and as carrier gas. The reactive molecular gases are usually avoided in order to achieve homogeneous nucleation and high chemical purity of the NPs. In some experiments, molecular gases are added, but mainly with respect to reactive chemical sputtering of the early transition metals.[32−37] The effort was aimed to affect the properties of individual NPs, such as composition and size distribution. To date, very few experimental or theoretical studies have been reported on effects of molecular gases on assembly of complexes of NPs with specific interparticle positioning. This is expected since the ligand-free surfaces of NPs tend to agglomerate the vicinal NPs due to formation of strong interatomic bonds, particularly, in the case of metallic NPs. However, in this work, we show that adding a small amount of weakly bound "ligands" helps to slow down the coalescence of NPs, kinetically trapping the system in

Received: August 11, 2020
Revised: October 7, 2020
Published: October 21, 2020

metastable configurations for tens of microseconds, affecting the results of final deposition.

This study is the first to present a single-step millisecond synthesis of Au core−satellite complexes in the presence of H_2O molecules. The similar liquid-phase synthesized core−satellite assemblies has been demonstrated for the promising applications such as chiral molecules detection,[38] microRNA detection,[39] and plasmonics.[40] We combine high-resolution spherical aberration corrected scanning transmission electron microscopy (C_s-corrected HR-STEM) and different state-of-the-art theoretical models ranging from classical molecular dynamics (MD) simulations to first-principles quantum mechanical calculations to elucidate the key mechanisms of how such complexes are formed.

Our MD simulations show that the H_2O molecules adsorb at the surface of Au NPs at room temperature. A single layer of water can bridge small NP and large ones, forming stable core−satellite complexes flying together. Dispersion interactions between water and Au NPs hold the system together even if NPs fly to the deposition zone rotating around themselves during the milliseconds of synthesis time. The HR-STEM analysis of the interparticle distance is in a remarkable agreement with the MD simulations. We also demonstrate that the aerodynamics of different size NPs in the aggregation zone is a key factor determining the size distribution of the deposited NPs. Moreover, an angular momentum of rotating particles explains a core−satellite composition of the complexes.

METHODS

Experimental Methods. All nanoparticles were grown using a 2 inches diameter full face erosion (FFE) magnetron (Nano4Energy SL) fitted into a standard gas aggregation source (GAS) (Oxford Applied Research Ltd.). The FFE magnetron that is made of rotating magnets generates a much more uniform erosion of the sputtering target and extends its lifetime,[25] while it also eliminates the well-known fluctuations of the NP generation caused by the racetrack formation in standard magnetrons.[41,42] Hence, a stable generation of NPs could be achieved for long periods of time. The magnetron was positioned at its longest aggregation distance (i.e., magnetron head at 100 mm from exit slit of aggregation zone) and a stable flux of argon (80 sccm) gas was injected through a mass flow controller at the back side of the aggregation zone. An additional pipeline (note that all pipelines are stainless steel pipes properly cleaned and baked-out) connected at the back side of the aggregation zone was equipped with an ultraprecise mass flow controller (step of 10^{-3} sccm) fitted with pure bottles of O_2, N_2, and a glass reservoir of Milli-Q H_2O whose water vapor generated at ambient temperature was injected into the aggregation zone. Also, small doses of air were injected through the mass flow controller into the aggregation zone. In the case of air, O_2, and N_2, doses of 0.1 and 0.2 sccm were injected, while in the case of H_2O, 0.015 sccm was injected. The base pressures measured in the GAS while injecting the gases were 5×10^{-7}, 4×10^{-6}, and 8×10^{-6} mbar for 0.015, 0.1, and 0.2 sccm, respectively, and the total pressure measured in the GAS after injecting all gases (air or O_2 or N_2 or H_2O and Ar) was 4×10^{-3} mbar. Therefore the proportion of injected gases (air, O_2 or N_2 or H_2O) was 1.25×10^{-4}, 1×10^{-3}, and 2×10^{-3} for 0.015, 0.1, and 0.2 sccm respectively.

The FFE magnetron was operated at a power of 90 W and a current of 0.21 A, and the NPs were collected in a ultrahigh vacuum chamber (base pressure in the high 10^{-10} mbar) connected to the GAS. Ultrathin carbon coated copper TEM grids located at a distance of 400 mm from the exit slit of the GAS were used as substrates were the NPs were soft-landed.[43] Electron microscopy observations were performed using a JEOL GrandARM operated in STEM mode at 300 kV. Due to the atomic number (Z) sensitivity, the data was recorded using a high-angle annular dark field (HAADF) detector, which allowed the clear visualization of the strong scattering Au NPs respect to the carbon support, which appeared almost invisible. By selecting this detector, the surface atoms of the NPs can be unambiguously imaged and diffraction phenomena are also minimized. The column was equipped with a double corrector from JEOL assuring a spatial resolution of 0.7 Å. The microscope was also equipped with a double JEOL EDS system, a Gatan Quantum energy filter, and a K2 camera.

Computational Method. *Classical Molecular Dynamics.* We have performed MD simulations aiming at three goals: (i) to understand the effect of water in the early nucleation stage, (ii) to elucidate the formation mechanism of the core−satellite structures experimentally observed, and (iii) to demonstrate the aerodynamics of NPs in the condensation chamber. We performed three different sets of simulations, which we refer in the remaining of the article as **Sim1**, **Sim2**, and **Sim3**.

In the set **Sim1**, we simulate the early stage of the nucleation of the Au NPs. Here we use the MD simulations, which are set to represent four different scenarios of Au nanocluster growth: (i) in a pure Ar atmosphere: 500 Au and 5000 Ar atoms; (ii) the Ar atmosphere with added 1 at % of water molecules (H_2O): 500 Au and 4950 Ar atoms, and 50 H_2O molecules; (iii) the Ar atmosphere with added 10 at % of H_2O: 500 Au and 4500 Ar atoms, and 500 H_2O molecules. The ratio of the Au atoms to Ar atoms was calculated according to the analytical equation in ref 44:

$$\frac{\rho_{Au}}{\rho_{Ar}} = \left(\frac{Y_{Au}^{Ar} I_d/e^-}{\phi_{Ar}\cdot P_{at}/P_{Ar}}\right)\Big/\left(\frac{P_{Ar}}{k_B T_{Ar}}\right) \quad (1)$$

where the Au sputtering yield, Y_{Au}^{Ar} = 1.33 at 380 eV from ref 45, I_d is the dc current, ϕ_{Ar} is the gas flow rate, P_{at} denotes the atmospheric pressure, T_{Ar} is the temperature of the gas phase, and k_B is the Boltzmann constant. The ratio of the Au atoms to Ar atoms is about 0.1 estimated from the experiments. In the model, both Ar and Au atoms are neutral and O−H bonds are inactive; therefore, only physical adsorption of water to gold is considered. We add much higher concentration water molecules than in experiment to enable faster dynamics of water condensation within the short MD time span. The isolated atoms and molecules are generated randomly in the simulation box of the size 20 nm × 20 nm × 20 nm, as shown in Figure 1a.

The number of Ar and Au atoms in the simulations of pure Ar atmosphere are 5000 and 500, respectively. To analyze the effect of the water admixture, 50 or 500 Ar atoms are replaced by H_2O molecules. Ten independent simulations for each ratio of Ar were carried out for more than 10 ns with an adaptive time step to ensure that the maximum distance for an atom to move within one MD step does not exceed 0.01 Å/step (see Supporting Information Figure S4).

In the set **Sim2**, we simulate the dynamics of interaction of two pairs of the already formed nanoparticles: the first pair consists of two spherical Au NPs of 426 and 55 atoms (Au426 and Au55, respectively), and the second includes two

https://dx.doi.org/10.1021/acs.jpcc.0c07346
J. Phys. Chem. C 2020, 124, 24441−24450

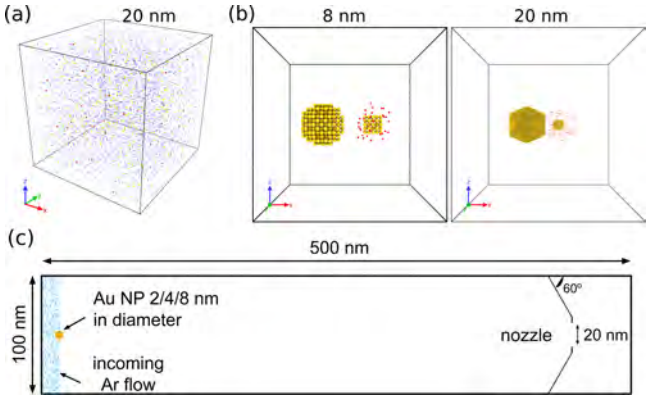

Figure 1. Summary of the initial setup of the three types of simulations. Ar atoms are in blue, Au in yellow, O in red, and H in gray: (a) nucleation simulations **Sim1**, (b) coalescence simulations **Sim2**, and (c) gas-flow simulations **Sim3**.

icosahedral NPs of 3871 and 147 atoms (Au3871 and Au147, respectively). The first pair is created inside of a $8 \times 8 \times 8$ nm^3 and the second inside of a $20 \times 20 \times 20$ nm^3 simulation cells with the periodic boundary condition applied in both cases. The initial distance between the closest points on the surfaces of the two corresponding NPs is 11.5 Å. The water molecules in both cases are added around the smallest NP within 10 Å from the surface and separated from one another by the distance of ≥2.0 Å. The number of molecules around the Au55 NP is approximately 30−40 and approximately 110−120 in the case of the Au147 NP (see Supporting Information Movie S1). The similar systems can be constructed such as core−double-satellite and core−core system, which will be discussed in detail in the Results and Discussion section.

We emulate the Brownian motion of the NPs within the inert gas condensation chamber in the simulation set **Sim3**. In the two-dimensional simulations, we are able to reach well beyond the time and length scales of a classical MD. The chamber is simulated as a 500 nm × 100 nm rectangle and is schematically shown in Figure 1c. A nozzle with the aperture of 20 nm in diameter is installed at 60° from the walls of the chamber at the distance of 50 nm from its end. The x and y axes are aligned with the longest and shortest sides of the box, respectively. Comparing with the corresponding experimental setup,[25] this simulation box can be considered as the very end of the condensation chamber. The forces and velocities in the z direction of all the atoms are set to zero. Initially, 700 Ar atoms are generated randomly within 0 and 105 Å along the x axis. A reflective wall at the x = 0 Å is used to ensure the flow of the gas atoms in one direction only. A single Au cluster of 2/4/8 nm in diameter is initially placed at edge of the Ar gas: (x, y) = (105 Å, 0 Å). About 7500 more Ar atoms are added in the same initial region after every 2000 MD steps to ensure the pressure gradient in the box. The initial velocities of the Ar atoms in random directions follow the Maxwell−Boltzmann distribution at 300 K, while the atoms of the Au NP are given the velocity of 20 m/s in the x direction. With this simulation setup, we perform 10 independent simulations for each size of a NP for 15 ns with a time step of 1 fs.

We employ the classical MD code LAMMPS[46] for the MD simulations in all three sets, while the results are visualized by OVITO.[47] The embedded atom method (EAM) is used to simulate Au−Au interaction,[48,49] while the interactions within the water molecules are simulated by the rigid TIP4P/2005[50] model. The long-distance Coulomb interactions are solved by means of the *pppm/tip4p* solver.[51] For the interaction between water molecules and Au clusters, we used both the modified

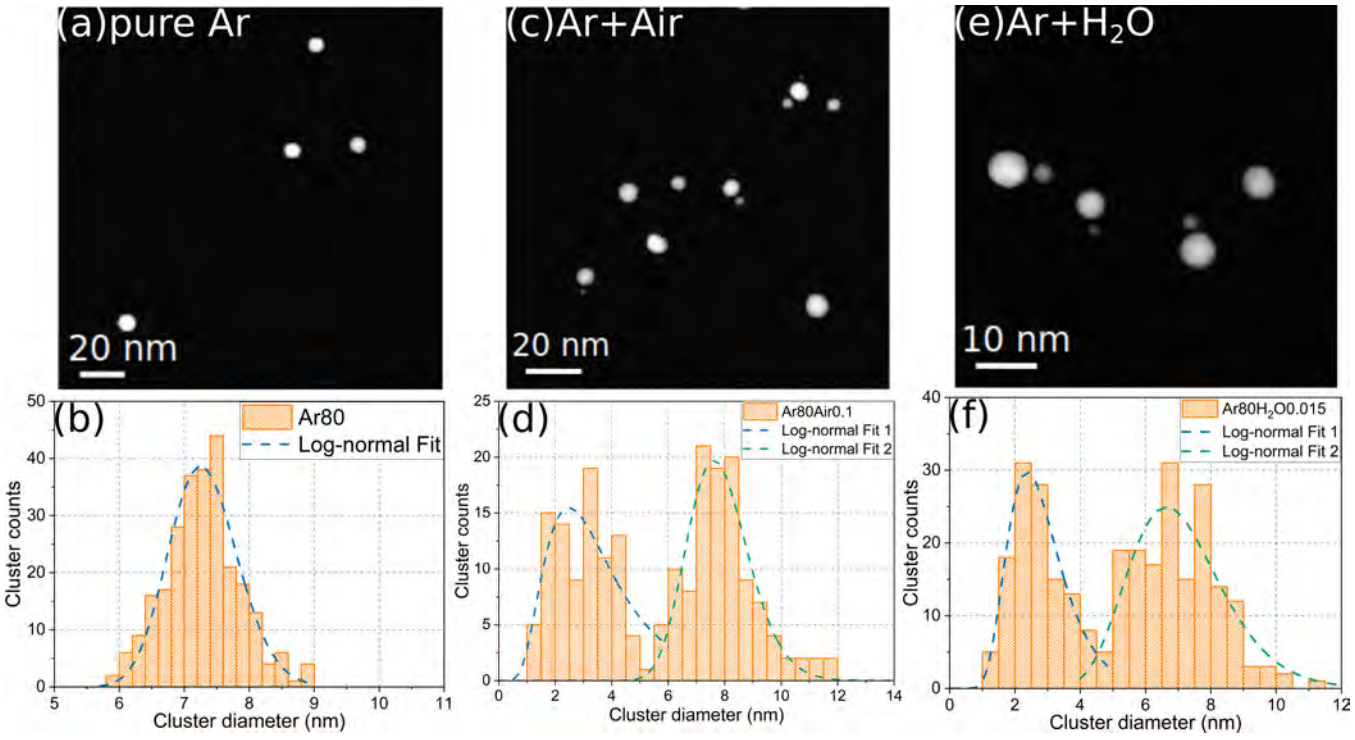

Figure 2. (a, c, e) C_s-corrected STEM-HAADF image and (b, d, f) the corresponding size-distribution analysis for Au NPs grown using (a, b) pure argon, (c, d) a mixture of air and pure argon, and (e, f) a mixture of H_2O and pure argon.

https://dx.doi.org/10.1021/acs.jpcc.0c07346
J. Phys. Chem. C 2020, 124, 24441−24450

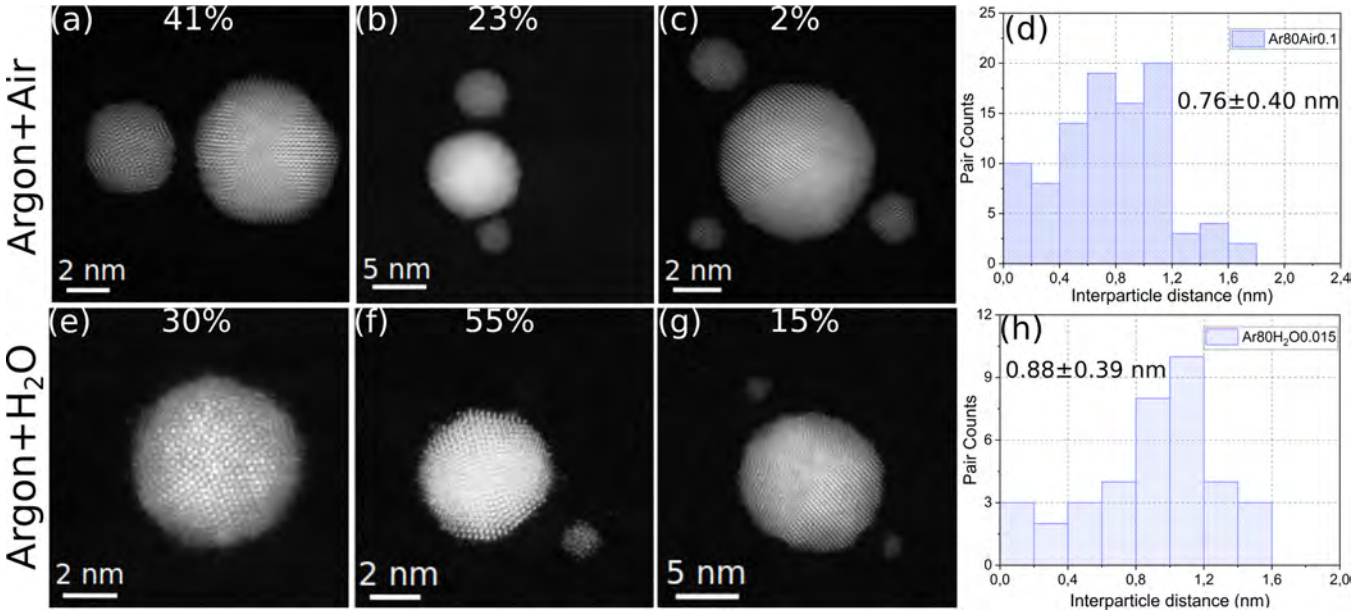

Figure 3. C_s-corrected STEM-HAADF images of exemplary core−satellite system in the case of Au NPs grown (a−c) with air and (e−g) with H_2O vapor. (d, h) Analysis of the interparticle distance between the big and small NPs. The statistics is preformed over 800 and 700 NPs, respectively. The percentage depicted in each figure is related to the proportion of big NPs in each configuration.

Spohr model[50] and a simplified 12-6 Lennard-Jones potential between the oxygen and gold atoms. The interaction between water molecules and gold NPs has been studied with molecular dynamics in liquid[52,53] and solid[54] phase previously. The results obtained from the two interactions were quite comparable. The Ar−Au and Ar−O interaction in the set **Sim1** were described by the repulsive Ziegler−Biersack−Littmark (ZBL)[55] potential to avoid surface adhesive of Ar atom.

Dispersion-Corrected Density Functional Theory Calculations. To investigate the strength of water adhesion to Au NPs, we further conduct first-principles calculations using the Vienna ab initio simulation package (VASP)[56,57] at the density functional theory level, employing the projected augmented wave (PAW) method[58] and the Perdew−Burke−Ernzerhof (PBE) functional.[59] To account for van der Waals interactions, we use Grimme's long-range dispersion correction (DFT-D3).[60]

In the DFT calculations, we expand the valence electronic states in the plane wave basis sets with an energy cutoff of 700 eV. We restrict the reciprocal space integration to the Γ-point only because of the large cluster system and no periodic boundary conditions. We choose 10^{-5} and 10^{-4} eV as the energy convergence criteria for optimization of the electronic and ionic structures, respectively. The Hellmann−Feynman forces are followed during the calculations.

The importance of non-covalent interactions between the water layer and the Au NPs is analyzed[61] using the promolecular approach as implemented in the NCIplot programme[62] and visualized using VMD.[63,64] For a quantitative estimate of the magnitude of dispersion interactions, we studied the Au_{426}/Au_{55} satellite pair, with a thin water layer of 35 water molecules in between, at the Geometries, vibrational Frequencies and Non-covalent eXtended Tight Binding (GFN1-xTB) level of theory.[65] The dispersion contribution was extracted at the DFT-D3 level of theory.[60] Three initial snapshot structures were taken from the MD trajectory. Keeping the Au NPs frozen, the geometry of the water molecules was optimized. Subsequently, average interaction energies were computed relative to a minimum structure of the $(H_2O)_{35}$ cluster, obtained by simulated annealing at the same level of quantum chemical theory.

RESULTS AND DISCUSSION

Experiments. In Figure 2a, we show a representative medium magnification C_s-corrected STEM-HAADF image of the Au NPs grown in pure Ar atmosphere. The corresponding size distribution fitted with a log-normal distribution[43,66] with a mean particle size around 7.2 ± 0.84 nm diameter is shown in Figure 2b. Higher magnification images of these NPs (see Figure S1 in the Supporting Information) reveal well-dispersed NPs of either decahedral or icosahedral morphology, with no sign of post-growth agglomeration or migration on the substrate. Figure 2c shows similar images of Au NPs, but grown in the mixture of 0.1 sccm of air and 80 sccm of pure argon. The presence of small NPs with the positioning in the close vicinity to a larger one is clearly observed in the latter image. The size distribution of these NPs (see Figure 2d) reveals a bimodal behavior with two distinct peaks corresponding to the mean diameters of 2.9 ± 1.02 and 7.7 ± 0.96 nm. (Additional STEM images with different magnifications can be found in Supporting Information Figure S2.)

Since the air admixture consists of different molecular gas components, it is not clear which of them may affect formation of the observed core−satellite complexes. Hence, we analyze separately the effect of the main air components, such as nitrogen, oxygen, and water vapor. We perform additional experiments for Au NPs growth in the Ar atmosphere injecting small quantities of the individual air component gases in the aggregation zone. While the admixture of pure nitrogen or pure oxygen did not promote formation of satellite structures, the results obtained with the traces of water vapor were strikingly similar to those obtained with the air admixture as presented in Figure 2e. In Figure 2f, we observe that the size

https://dx.doi.org/10.1021/acs.jpcc.0c07346
J. Phys. Chem. C 2020, 124, 24441−24450

distribution of the deposited NPs grown with the water vapor admixture exhibits also a bimodal behavior with two clear maxima at 2.60 ± 0.80 and 6.7 ± 1.50 nm corresponding to the mean diameters of the small and large NPs, respectively. In the analysis of over 700 NPs, we found again that about 99% of the small NPs are bound in core−satellite complexes. (Additional STEM images with different magnifications can be found in Supporting Information Figure S3.)

To quantify the presence of small NPs and their location with respect to the large ones, we analyzed the STEM images of over 800 NPs. The analysis revealed that about 99% of all the small NPs in the studied images were found as satellites around the big ones. We barely saw any isolated NPs with the diameter of ≤3 nm. In Figure 3a−c, we show different typical core−satellite complexes of a large NP (core) surrounded by the small ones (satellites), which were found in the images. The frequency of the appearance of each complex is specified on the corresponding image as percent with respect to the all studied NPs. The structure of both types of NPs was always found to adopt icosahedral or decahedral morphology, which are two common misfits of Au NPs in gas-phase condensation.[67−70] The majority of the core−satellite complexes includes either one and two satellite NPs. Formation of a trisatellite complex is relatively rare (2%). The distribution of the interparticle distances measured for all core−satellite complexes is centered at 0.76 ± 0.4 nm regardless of the size and the number of the satellites, as shown in Figure 3d. This observation contradicts to the hypothesis of the balance of Coulomb and centrifugal forces that keeps the NPs in close vicinity as recently proposed in ref 71. For this hypothesis to hold, the mass-to-charge ratio must affect the interparticle distance, which, as we show later, is not the case for the Au NPs.

The similarity of the results, which we obtain by injection of air and pure water vapor and the significant difference of these results from those obtained by injection of pure nitrogen and pure oxygen, suggest that the formation of core−satellite complexes is explained by the presence of water. The similarity between the air and water vapor injection results can further be seen in comparison of Figure 3a−d and Figure 3e−h. The average interparticle distance in the experiments with water vapor is 0.88 ± 0.39 nm, which is within the error bars of the same quantity estimated for the core−satellite complexes in experiments with air admixture.

In short conclusion, our experimental results evidence that the Au NPs core−satellites form only in the presence of H_2O molecules. To shed light on mechanisms governing this process, we further focus now on theoretical analysis of the effect of water vapor admixture on the process of growth of Au NPs.

Computational Simulations on the Formation Mechanism. The growth of NPs by gas-phase synthesis is governed by surface sputtering, nucleation kinetics, coalescence, aerodynamics as well as deposition processes. Molecular gas admixture may play an essential role at any of these stages. By using different computational techniques, we focus on three key steps of the growth process, which are driven by different mechanisms, in order to understand the pinpoint the role of water on growth dynamics.

First, we analyze the effect of H_2O molecules on the nucleation process of Au NPs. The results of these simulations, however, did not reveal any significant effect of the presence of water molecules in the condensation atmosphere on the early stage nucleation rate. Some snapshots of these simulations as well as the evolution dynamics of the atomic percent of Au mono-, di-, tri-, and tetramers can be found in Figures S4 and S5 of the Supporting Information. Since the temperature of the initial nuclei is much above 800 K, these results are well in line with the experimental observations, which showed that water does not to bind to Au nuclei above 800 K.[72] However, at the temperature below 500 K, the water molecules were shown to condense on the surface of Au NPs. In our simulations, we also observe that, after the temperature is reduced, a water layer condenses around the NP. This layer may serve as a buffer preventing the two Au NPs from coalescence or separating from each other. Therefore, it is plausible to assume that the core−satellite complexes may be formed due to water condensation on NPs during the last stage of particle agglomeration, when the temperature of the Au NPs is sufficiently low to allow the physisorption of water molecules.

The dynamics of pairwise interaction between a big and a small Au NPs were simulated at lower temperatures. We obtained the statistically significant results by carrying out 15 and 10 independent simulations at 288 and 400 K, respectively. In the simulations performed at 288 K, the water molecules initially condense as a single layer around the small NP during the first 50 ps. However, the vicinity of the large NP attracts the water molecules, which gather at the side of the small NP, which is closer to the large one. Eventually, the water layer stabilizes between the two NPs forming a buffer layer that prevents them from completing the coalescence. The snapshot shown in Figure 4a illustrates the process of formation of a water buffer layer between two icosahedral NPs, Au_{3871} and Au_{147}. The whole process of formation of a water buffer layer in these simulations can be found in Supporting Information Movie S1. The average interparticle distance in these simulations is found to be 0.7 ± 0.02 nm, which can be directly compared with the STEM images as shown in Figure 4b. The core−satellite complex survived as a whole in 12 out of 15 independent cases. Similar results were observed in the simulations with the smaller spherical Au_{426} and Au_{55} NPs.

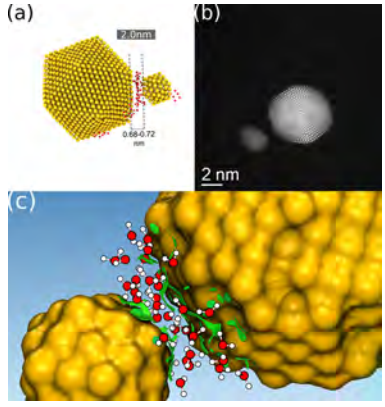

Figure 4. (a) Cross-sectional images from Simulations type **Sim2** at 288 K. (b) Typical experimental image of a core−satellite NP system. The interparticle distance of 0.7 ± 0.02 nm is in very good agreement with those found experimentally. (c) Non-covalent interactions between the water layer and the gold NPs in a snapshot of the $Au_{426}/(H_2O)_{35}/Au_{55}$ system.

In the simulations performed at 400 K, only a fraction of water molecules remains adsorbed at the small NP. However,

https://dx.doi.org/10.1021/acs.jpcc.0c07346
J. Phys. Chem. C 2020, 124, 24441−24450

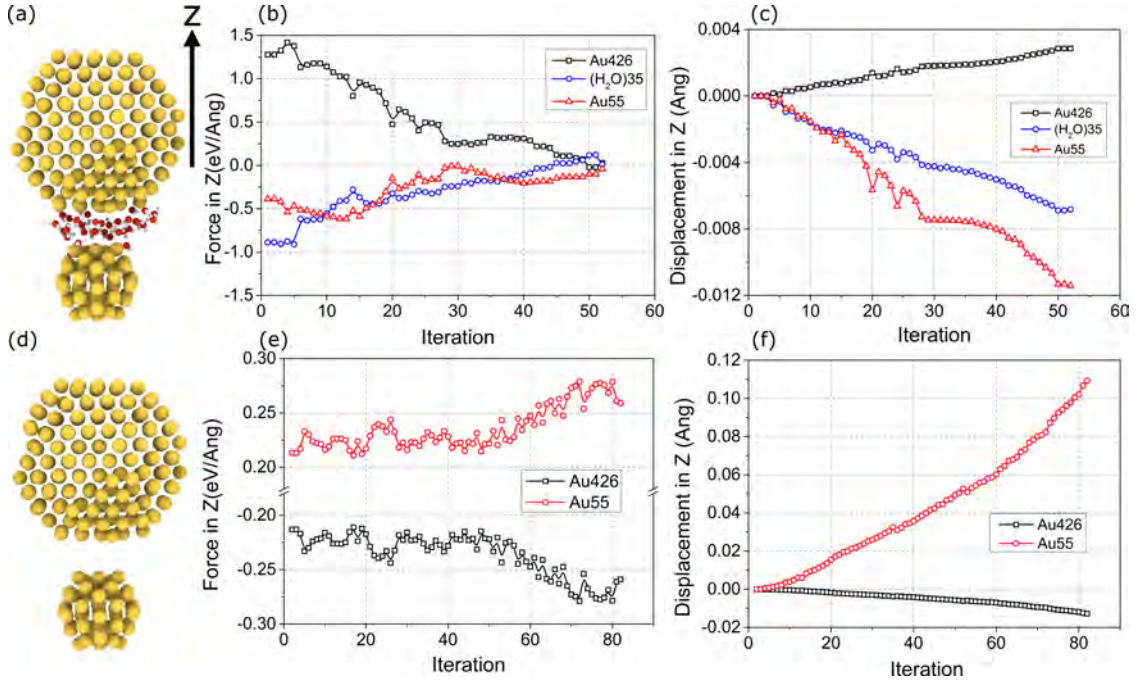

Figure 5. DFT-D3 calculation: (a) the complex of two NPs, Au_{426} and Au_{55} separated by 35 H_2O molecules; (d) the same complex without presence of water. Panels (b) and (e) show the total net forces in the *Z* direction of each part, Au_{426}, water layer, and Au_{55}. Panels (c) and (f) show the displacement of the center of mass of each part comparing to the initial positions.

at the elevated temperature, the water layer becomes unstable, and the screening of interactions between the two Au NPs is less efficient. Consequently, the NPs merged into a single one after 1 ns in all simulated cases.

Moreover, we analyze the effect of the size of the constituent NPs in two additional structures: (i) core−double-satellites include Au_{3871}, two Au_{147} NPs, and 195 H_2O molecules in between; (ii) core−core complex includes two Au_{3871} NPs and 174 H_2O molecules in between. The core−double-satellite complex survived until the end of the simulations in one out of five independent runs, while the core−core complex survived in two out of five runs. In all runs, where the NPs within complexes remained connected, the simulation was run for 1 ns at 288 K.

Applying dispersion corrected density functional theory calculations (PBE-D3), we verify the stability of a core−satellite complex held together by a water layer. We relax the final frame of one of the $Au_{426}/(H_2O)_{35}/Au_{55}$ MD simulations toward a local minimum using the conjugate gradient method.[73] For a reference, we consider a similar system Au_{426}/Au_{55}, but without water. Figure 5a,d shows the snapshots of the relaxed structures with and without a water layer, respectively. In Figure 5b,e, we monitor the evolution of the forces in the corresponding complexes, while Figure 5c,f shows the displacements of the centers of mass of the complexes shown in Figure 5a,d, respectively, along the *z* axis during the relaxation.

Comparison of the forces acting on the NPs within the two relaxed complexes with and without the interparticle water layer (Figure 5b,e, respectively) reveals the effect of the water layer on the interaction between the two metal NPs. In Figure 5b, the water layer screens attraction of the small satellite NP to the large core NP since the forces in Figure 5b eventually converged to zero. While the forces acting on two NPs without a water layer only increase with the number of iterations, as it is shown in Figure 5e. This result is also consistent with the analysis of the displacements of the centers of mass of Au_{426} and Au_{55} during the relaxation runs as shown in Figure 5c,f. In the presence of the water layer, the calculation iterations lead to a further separation of the particles by an insignificant distance of ∼0.016 Å. In the system without a water layer, the distance between the two NPs is rapidly decreasing and by the end of the calculations, it amounts to 0.13 Å, see Figure 5f. In these calculations, the forces increase from 0.21 to 0.25 eV/Å, indicating the formation of a metallic bond between the two gold clusters. Strong forces will inevitably bring two clusters together, resulting in coalescence event, which we observe in our MD simulations.

Dispersion interactions are crucial for formation of a water layer and, thereby, for the whole screening mechanism. Figure 4c shows the results of the analysis of noncovalent interactions in the $Au_{426}/(H_2O)_{35}/Au_{55}$ system. Dispersion interactions are shown as green areas between the water and the Au NPs. For a small $(H_2O)_{35}$ cluster to adsorb on the surface of a Au NP, a large fraction of hydrogen bonds needs to be broken. Without dispersion interaction, the wetting process can become prohibitively endothermic. However, our quantum chemical level calculations using the Geometries, vibrational Frequencies and Noncovalent interactions eXtended Tight Binding (GFN-xTB) method indicate the attractive interaction energy between the water layer and the two Au NPs of ∼1.2 eV as compared to the system of a free standing $(H_2O)_{35}$ cluster and two Au NPs at the same separation. We estimate the dispersion interactions between the water molecules and the Au NPs to be ∼5.1 eV. Hence, these calculations confirm that the physisorption of a small water cluster of $(H_2O)_{35}$ is an energetically favorable process.

Aerodynamics and Angular Momentum. Both our MD simulations and DFT calculations corroborate experimental observation and confirm that the role of H_2O molecules is

https://dx.doi.org/10.1021/acs.jpcc.0c07346
J. Phys. Chem. C 2020, 124, 24441−24450

essential in the formation of core−satellite complexes. If so, one may expect seeing small Au NPs well separated from the big ones. However, only very few small NPs were found in STEM images, which are shown in Figure 2a,c,e, and persistently in the vicinity of the large ones. To understand the reason for such selective separation, we perform yet the third type of simulations, where we study the drift trajectories of the NPs with different sizes in the flow of the carrier gas of the condensation chamber. We track the trajectories (green lines in Figure 6) of 10 independent NPs of 2, 4, and 8 nm in diameter that are placed at the beginning of the chamber vertically aligned with the center of the nozzle, which leads the NPs to the deposition substrate. In each simulation, the NP is given an initial drift velocity 20 m/s toward the center of the nozzle. Without collisions with the atoms of the Ar atmosphere, all NPs will pass through the nozzle at a straight line. We create the carrier gas flow by maintaining the Ar gas pressure at the beginning of the condensation chamber and removing the Ar atoms, which reached the region behind the nozzle.

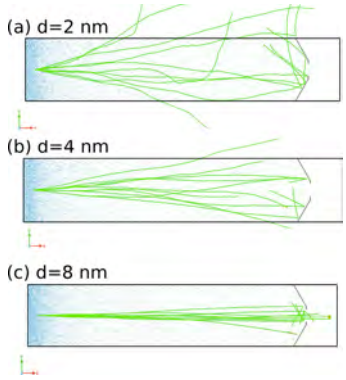

Figure 6. Drift trajectories of two-dimensional NPs with (a) 2.0, (b) 4.0, and (c) 8.0 nm in diameter.

The simulations show that the small NPs experience stronger collisions with the carrier gas atoms, diverging significantly from the straight line. As a result, we found that none of the 10 2 nm NPs managed to pass the nozzle, while 4 out of then 10 8 nm NPs passed the nozzle almost without diverging from the initial straight line. A similar effect has been studied, for instance, in macroscopic aerodynamics simulations.[74] The results indicate that the increased number of small NPs among those grown with the water admixture is explained by the formation of the core−satellite complexes inside of the condensation chamber, which are able to bring the small NPs through the nozzle. It also explains the fact that few isolated small NPs were seen in all experimental images.

Moreover, we note that a water buffer layer may also form between two large NPs, landing side-by-side on a substrate. However, it is very rare to see in the TEM images of the current experiments a pair of closely positioned NPs of identical size. Two explanations of this result are plausible: First, it is known that the length of the mean free path of a large NP is of the same magnitude as the dimension of the aggregation zone; therefore, the probability of two large NPs of similar size to meet in a very close vicinity to one another is very low. Second, we note that the particles do not fly through the entire aggregation zone without rotation. The multiple random impacts with Ar atoms will not only change the direction of the trajectory but also give rise to the angular momentum in motion of a NP or a formed core−satellite system. The centrifugal force due to such angular momentum may be considered as an additional factor explaining a specific large core−small satellite complex. As suggested in ref 71, the angular momentum of the core−satellite system can be fairly large. To analyze this effect, we run two simulations to probe the maximal rotational speed for the core−satellite and core−core complexes.

In these simulations, we follow the rotational dynamics of the Au NP complexes, one of which has one core and two satellite NPs and another two identical cores. The structures were relaxed in the **Sim2** simulations at 288 K. The angular momenta are added to all atoms within the complexes as an additional velocity $v = \omega \times r_i$, where ω is the target angular velocity and r_i is the radius vector from the center of mass of the system to the atom i. The thermal velocities of atoms are not scaled because of the angular component, so the total angular momentum remains conserved during the simulation. The detailed evolution of the separation of the NPs of the core−satellite and core−core complexes can be found in the Supporting Information as Movie S2 and Movie S3, respectively. Figure 7 shows the snapshots of the representative states in the three simulations, which we performed with the core−double-satellite (i) and core−core (ii) as described above. These simulations show that the linear velocities of the system with satellites can reach the values as high as 250 m/s before the system will break apart because of the centrifugal force. The complexes of two similar size cores break apart at much lower linear velocity of ≈110 m/s as in our example. Therefore, we conclude that the core−core system is improbable first due to significant mean free path that would prevent the formation of the structure, but even if such a structure was formed, the stability of it is in question because of a significant centrifugal force acting on both particles from the center of mass of the system, which coincides with the position of separating water layer.

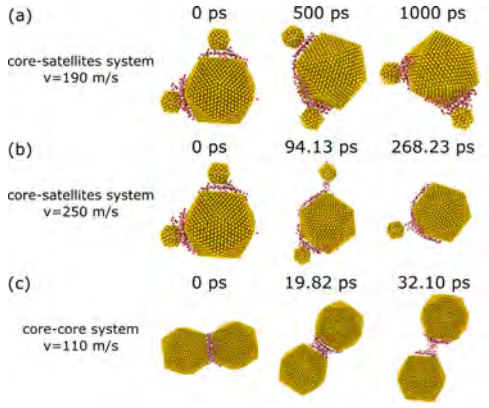

Figure 7. Snapshots of the rotational MD simulations: (a, b) Au_{3871} core with two Au_{147} satellites and about 100 H_2O per a satellite; (c) two Au_{3871} cores with 174 H_2O molecules in between. The linear velocities shown to the left were initially assigned to all atoms in corresponding complex: cases (a), (b), and (c) are 190, 250, and 110 m/s, respectively. In case (a), the complex survived until the end of the 1 ns of the simulated time, while in cases (b) and (c), the complex felt apart at 268.23 at 32.10 ps, respectively.

https://dx.doi.org/10.1021/acs.jpcc.0c07346
J. Phys. Chem. C 2020, 124, 24441−24450

CONCLUSIONS

In summary, we demonstrate a gas-phase-based synthesis approach of Au core−satellite nanoparticle complexes by a magnetron sputtering inert gas condensation approach with water vapor admixture. Furthermore, we develop a detailed multistep model to explain the kinetic formation mechanism of these complex structures. The direct comparison of the experimental STEM images and the results of our MD simulations show a very good agreement between theory and experiment. The results indicate that core−satellite complexes form only during the low-temperature stage, when the water molecules adsorb on Au NPs. Small NPs adhered with a water layer to the large ones are carried by the latter to the deposition substrate along the more stable trajectories. Higher concentrations of H_2O admixture in the later stage of the concentration process and more efficient cooling are expected to further promote the stability of the core−satellite structures. The results strongly suggest that considering water as an admixture in the inert gas condensation opens up possibilities of controlling the final configuration of the different noble metal NPs such as platinum, palladium, and silver.

ASSOCIATED CONTENT

Supporting Information

The Supporting Information is available free of charge at https://pubs.acs.org/doi/10.1021/acs.jpcc.0c07346.

Additional STEM images with different magnifications and additional snapshots and analysis of the simulation set **Sim1** (PDF)

Movie S1: Formation and stabilization of the core−satellite structure with single-layer water molecules (MP4)

Movie S2: Rotational motion that causes the separation of core and satellites (MP4)

Movie S3: Rotational motion that causes the separation of the two big NPs (MP4)

AUTHOR INFORMATION

Corresponding Authors

Junlei Zhao − *Department of Physics and Helsinki Institute of Physics, University of Helsinki, FIN-00014 Helsinki, Finland; Department of Electrical and Electronic Engineering, Southern University of Science and Technology, Shenzhen 518055, China;* orcid.org/0000-0002-4919-2440; Email: zhaojl@sustech.edu.cn

Flyura Djurabekova − *Department of Physics and Helsinki Institute of Physics, University of Helsinki, FIN-00014 Helsinki, Finland;* orcid.org/0000-0002-5828-200X; Email: flyura.djurabekova@helsinki.fi

Yves Huttel − *Materials Science Factory, Instituto de Ciencia de Materiales de Madrid (ICMM-CSIC), 28049 Madrid, Spain*; Email: huttel@icmm.csic.es

Authors

Alvaro Mayoral − *Institute of Nanoscience and Materials of Aragon (INMA), Spanish National Research Council (CSIC) and Laboratorio de Microscopias Avanzadas (LMA), University of Zaragoza, 50009 Zaragoza, Spain; Center for High-Resolution Electron Microscopy (ChEM) School of Physical Science and Technology, ShanghaiTech University, Shanghai 201210, China;* orcid.org/0000-0002-5229-2717

Lidia Martínez − *Materials Science Factory, Instituto de Ciencia de Materiales de Madrid (ICMM-CSIC), 28049 Madrid, Spain*

Mikael P. Johansson − *Department of Chemistry, University of Helsinki, FI-00014 Helsinki, Finland; CSC−IT Center for Science, FI-02101 Espoo, Finland;* orcid.org/0000-0002-9793-8235

Complete contact information is available at: https://pubs.acs.org/10.1021/acs.jpcc.0c07346

Notes

The authors declare no competing financial interest.

ACKNOWLEDGMENTS

Computational research performed at the University of Helsinki was supported by the EU project M4F (project ID: 755039), the Academy of Finland (projects 289179 and 319453), and Waldemar von Frenckells sitftelse. The Finnish IT Center for Science (CSC), the Finnish Grid and Cloud Infrastructure (urn:nbn:fi:research-infras-2016072533) provided computational resources. The computational work was also supported by Center for Computational Science and Engineering at Southern University of Science and Technology. The experimental work was supported by the Spanish Ministerio de Ciencia e Innovación under project no. MAT2014-59772-C2-2-P and by the European ERC-2013-SyG 610256 grant. A.M. acknowledges the Center of High-resolution Electron Microscopy, ChEM, supported by SPST of ShanghaiTech University under contract no. EM02161943 and the Natural National Science Foundation of China (NSFC) NSFC-21850410448 and NSFC-21835002. A.M. also acknowledges the Spanish Ministry of Science under the Ramon y Cajal Program (RYC2018-024561-I).

REFERENCES

(1) Vernieres, J.; Steinhauer, S.; Zhao, J.; Chapelle, A.; Menini, P.; Dufour, N.; Diaz, R. E.; Nordlund, K.; Djurabekova, F.; Grammatikopoulos, P.; et al. Gas Phase Synthesis of Multifunctional Fe-Based Nanocubes. *Adv. Funct. Mater.* **2017**, *27*, 1605328.

(2) Zanolli, Z.; Leghrib, R.; Felten, A.; Pireaux, J.-J.; Llobet, E.; Charlier, J.-C. Gas Sensing with Au-Decorated Carbon Nanotubes. *ACS Nano* **2011**, *5*, 4592−4599.

(3) Atwater, H. A.; Polman, A. Plasmonics for improved photovoltaic devices. *Nature Mater.* **2010**, *9*, 205−213.

(4) Narayanan, R.; El-Sayed, M. A. Catalysis with Transition Metal Nanoparticles in Colloidal Solution: Nanoparticle Shape Dependence and Stability. *J. Phys. Chem. B* **2005**, *109*, 12663−12676.

(5) Lee, I.; Delbecq, F.; Morales, R.; Albiter, M. A.; Zaera, F. Tuning selectivity in catalysis by controlling particle shape. *Nature Mater.* **2009**, *8*, 132−138.

(6) Dumestre, F.; Chaudret, B.; Amiens, C.; Renaud, P.; Fejes, P. Superlattices of Iron Nanocubes Synthesized from Fe[N(SiMe3)2]2. *Science* **2004**, *303*, 821−823.

(7) Grzelczak, M.; Vermant, J.; Furst, E. M.; Liz-Marzán, L. M. Directed Self-Assembly of Nanoparticles. *ACS Nano* **2010**, *4*, 3591−3605.

(8) Liu, W.; Halverson, J.; Tian, Y.; Tkachenko, A. V.; Gang, O. Self-organized architectures from assorted DNA-framed nanoparticles. *Nat. Chem.* **2016**, *8*, 867−873.

(9) Zhu, H.; Fan, Z.; Yu, L.; Wilson, M. A.; Nagaoka, Y.; Eggert, D.; Cao, C.; Liu, Y.; Wei, Z.; Wang, X.; et al. Controlling nanoparticle orientations in the self-assembly of patchy quantum dot-gold heterostructural nanocrystals. *J. Am. Chem. Soc.* **2019**, *141*, 6013−6021.

(10) Chen, H.; Hu, H.; Tao, C.; Clauson, R. M.; Moncion, I.; Luan, X.; Hwang, S.; Sough, A.; Sansanaphongpricha, K.; Liao, J.; et al. Self-assembled Au@ Fe core/satellite magnetic nanoparticles for versatile biomolecule functionalization. *ACS Appl. Mater. Interfaces* **2019**, *11*, 23858−23869.
(11) Sanjeeva, K. B.; Pigliacelli, C.; Gazzera, L.; Dichiarante, V.; Bombelli, F. B.; Metrangolo, P. Halogen bond-assisted self-assembly of gold nanoparticles in solution and on a planar surface. *Nanoscale* **2019**, *11*, 18407−18415.
(12) Jahanmahin, O.; Kirby, D. J.; Smith, B. D.; Albright, C. A.; Gobert, Z. A.; Keating, C. D.; Fichthorn, K. A. Assembly of Gold Nanowires on Gold Nanostripe Arrays: Simulation and Experiment. *J. Phys. Chem. C* **2020**, *124*, 9559−9571.
(13) Baker, S. H.; Thornton, S. C.; Keen, A. M.; Preston, T. I.; Norris, C.; Edmonds, K. W.; Binns, C. The construction of a gas aggregation source for the preparation of massselected ultrasmall metal particles. *Rev. Sci. Instrum.* **1997**, *68*, 1853.
(14) von Issendorff, B.; Palmer, R. E. A new high transmission infinite range mass selector for cluster and nanoparticle beams. *Rev. Sci. Instrum.* **1999**, *70*, 4497.
(15) Krishnan, G.; Verheijen, M. A.; ten Brink, G. H.; Palasantzas, G.; Kooi, B. J. Tuning structural motifs and alloying of bulk immiscible Mo-Cu bimetallic nanoparticles by gas-phase synthesis. *Nanoscale* **2013**, *5*, 5375−5383.
(16) Llamosa Pérez, D.; Espinosa, A.; Martínez, L.; Román, E.; Ballesteros, C.; Mayoral, A.; García-Hernández, M.; Huttel, Y. Thermal diffusion at nanoscale: from CoAu alloy nanoparticles to Co@Au core/shell structures. *J. Phys. Chem. C* **2013**, *117*, 3101−3108.
(17) Llamosa, D.; Ruano, M.; Martínez, L.; Mayoral, A.; Roman, E.; García-Hernández, M.; Huttel, Y. The ultimate step towards a tailored engineering of core@shell and core@shell @shell nanoparticles. *Nanoscale* **2014**, *6*, 13483−13486.
(18) Benelmekki, M.; Bohra, M.; Kim, J.-H.; Diaz, R. E.; Vernieres, J.; Grammatikopoulos, P.; Sowwan, M. A facile single-step synthesis of ternary multicore magneto-plasmonic nanoparticles. *Nanoscale* **2014**, *6*, 3532−3535.
(19) Plant, S. R.; Cao, L.; Palmer, R. E. Atomic Structure Control of Size-Selected Gold Nanoclusters during Formation. *J. Am. Chem. Soc.* **2014**, *136*, 7559−7562.
(20) Yin, C.; Tyo, E.; Kuchta, K.; von Issendorff, B.; Vajda, S. Atomically precise (catalytic) particles synthesized by a novel cluster deposition instrument. *J. Chem. Phys.* **2014**, *140*, 174201.
(21) Zhao, J.; Baibuz, E.; Vernieres, J.; Grammatikopoulos, P.; Jansson, V.; Nagel, M.; Steinhauer, S.; Sowwan, M.; Kuronen, A.; Nordlund, K.; et al. Formation mechanism of Fe nanocubes by magnetron sputtering inert gas condensation. *ACS Nano* **2016**, *10*, 4684−4694.
(22) Martínez, L.; Mayoral, A.; Espiñeira, M.; Roman, E.; Palomares, F. J.; Huttel, Y. Core@shell, Au@TiOx nanoparticles by gas phase synthesis. *Nanoscale* **2017**, *9*, 6463−6470.
(23) Mayoral, A.; Llamosa, D.; Huttel, Y. A novel Co@Au structure formed in bimetallic core@shell nanoparticles. *Chem. Commun.* **2017**, *51*, 8442−8445.
(24) Vahl, A.; Strobel, J.; Reichstein, W.; Polonskyi, O.; Strunskus, T.; Kienle, L.; Faupel, F. Single target sputter deposition of alloy nanoparticles with adjustable composition via a gas aggregation cluster source. *Nanotechnol.* **2017**, *28*, 175703.
(25) Huttel, Y.; Martínez, L.; Mayoral, A.; Fernández, I. Gas-phase synthesis of nanoparticles: present status and perspectives. *MRS Commun.* **2018**, *8*, 947−954.
(26) Mayoral, A.; Martínez, L.; García-Martín, J. M.; Fernández-Martínez, I.; García-Hernández, M.; Galiana, B.; Ballesteros, C.; Huttel, Y. Tuning the size, composition and structure of Au and $Co_{50}Au_{50}$ nanoparticles by high-power impulse magnetron sputtering in gas-phase synthesis. *Nanotechnol.* **2019**, *30*, No. 065606.
(27) Huttel, Y., Ed. *Gas-Phases Synthesis of Nanoparticles*; Wiley, 2017.
(28) Liao, T.-W.; Yadav, A.; Hu, K.-J.; van Der Tol, J.; Cosentino, S. L.; D'Acapito, F.; Palmer, R. E.; Lenardi, C.; Ferrando, R.; Grandjean, D.; et al. Unravelling the nucleation mechanism of bimetallic nanoparticles with composition-tunable core−shell arrangement. *Nanoscale* **2018**, *10*, 6684−6694.
(29) Vernieres, J.; Steinhauer, S.; Zhao, J.; Grammatikopoulos, P.; Ferrando, R.; Nordlund, K.; Djurabekova, F.; Sowwan, M. Site-Specific Wetting of Iron Nanocubes by Gold Atoms in Gas-Phase Synthesis. *Adv. Sci.* **2019**, *6*, 1900447.
(30) Mattei, J.-G.; Grammatikopoulos, P.; Zhao, J.; Singh, V.; Vernieres, J.; Steinhauer, S.; Porkovich, A.; Danielson, E.; Nordlund, K.; Djurabekova, F.; Sowwan, M. Gas-Phase Synthesis of Trimetallic Nanoparticles. *Chem. Mater.* **2019**, *31*, 2151−2163.
(31) Zhao, J.; Singh, V.; Grammatikopoulos, P.; Cassidy, C.; Aranishi, K.; Sowwan, M.; Nordlund, K.; Djurabekova, F. Crystallization of Silicon Nanoclusters with Inert Gas Temperature Control. *Phys. Rev. B* **2015**, *91*, No. 035419.
(32) Shyjumon, I.; Gopinadhan, M.; Helm, C. A.; Smirnov, B. M.; Hippler, R. Deposition of titanium/titanium oxide clusters produced by magnetron sputtering. *Thin Solid Films* **2006**, *500*, 41−51.
(33) Ahadi, A. M.; Zaporojtchenko, V.; Peter, T.; Polonskyi, O.; Strunskus, T.; Faupel, F. Role of oxygen admixture in stabilizing TiO_x nanoparticle deposition from a gas aggregation source. *J. Nanopart. Res.* **2013**, *15*, 2125.
(34) Peter, T.; Polonskyi, O.; Gojdka, B.; Mohammad Ahadi, A.; Strunskus, T.; Zaporojtchenko, V.; Biederman, H.; Faupel, F. Influence of reactive gas admixture on transition metal cluster nucleation in a gas aggregation cluster source. *J. Appl. Phys.* **2012**, *112*, 114321.
(35) Chamorro-Coral, W.; Caillard, A.; Brault, P.; Andreazza, P.; Coutanceau, C.; Branton, S. The role of oxygen on the growth of palladium clusters synthesized by gas aggregation source. *Plasma Processes Polym.* **2019**, *16*, No. e1900006.
(36) Marek, A.; Valter, J.; Kadlec, S.; Vyskočil, J. Gas aggregation nanocluster source— reactive sputter deposition of copper and titanium nanoclusters. *Surf. Coat. Technol.* **2011**, *205*, S573−S576.
(37) De Toro, J. A.; Andrés, J. P.; González, J. A.; Riveiro, J. M.; Estrader, M.; López-Ortega, A.; Tsiaoussis, I.; Frangis, N.; Nogués, J. Role of the oxygen partial pressure in the formation of composite Co-CoO nanoparticles by reactive aggregation. *J. Nanopart. Res.* **2011**, *13*, 4583−4590.
(38) Zhang, Y.; Liu, J.; Li, D.; Dai, X.; Yan, F.; Conlan, X. A.; Zhou, R.; Barrow, C. J.; He, J.; Wang, X.; et al. Self-Assembled Core−Satellite Gold Nanoparticle Networks for Ultrasensitive Detection of Chiral Molecules by Recognition Tunneling Current. *ACS Nano* **2016**, *10*, 5096−5103.
(39) Meng, D.; Ma, W.; Wu, X.; Xu, C.; Kuang, H. DNA-Driven Two-Layer Core−Satellite Gold Nanostructures for Ultrasensitive MicroRNA Detection in Living Cells. *Small* **2020**, *16*, 2000003.
(40) Yoon, J. H.; Lim, J.; Yoon, S. Controlled assembly and plasmonic properties of asymmetric core−satellite nanoassemblies. *ACS Nano* **2012**, *6*, 7199−7208.
(41) Ganeva, M.; Pipa, A. V.; Hippler, R. The influence of target erosion on the mass spectra of clusters formed in the planar DC magnetron sputtering source. *Surf. Coat. Technol.* **2012**, *213*, 41−47.
(42) Rai, A.; Mutzke, A.; Bandelow, G.; Schneider, R.; Ganeva, M.; Pipa, A. V.; Hippler, R. Operational limit of a planar DC magnetron cluster source due to target erosion. *Nucl. Instrum. Methods Phys. Res., Sect. B* **2013**, *316*, 6−12.
(43) Díaz, M.; Martínez, L.; Ruano, M. M.; Llamosa, D.; Román, E.; García-Hernandez, M.; Ballesteros, C.; Fermento, R.; Cebollada, A.; Armelles, G.; Huttel, Y. Morphological, structural, and magnetic properties of Co nanoparticles in a silicon oxide matrix. *J. Nanopart. Res.* **2011**, *13*, 5321−5333.
(44) Quesnel, E.; Pauliac-Vaujour, E.; Muffato, V. Modeling Metallic Nanoparticle Synthesis in a Magnetron-Based Nanocluster Source by Gas Condensation of a Sputtered Vapor. *J. Appl. Phys.* **2010**, *107*, No. 054309.

https://dx.doi.org/10.1021/acs.jpcc.0c07346
J. Phys. Chem. C 2020, 124, 24441−24450

(45) Matsunami, N.; Yamamura, Y.; Itikawa, Y.; Itoh, N.; Kazumata, Y.; Miyagawa, S.; Morita, K.; Shimizu, R.; Tawara, H. *Energy Dependence of the Yields of Ion-Induced Sputtering of Monatomic Solids*. Nagoya University, 1983.
(46) Plimpton, S. Fast parallel algorithms for short-range molecular dynamics. *J. Comput. Phys.* **1995**, *117*, 1−19.
(47) Stukowski, A. Visualization and analysis of atomistic simulation data with OVITO−the Open Visualization Tool. *Modell. Simul. Mater. Sci. Eng.* **2009**, *18*, No. 015012.
(48) Foiles, S. M.; Baskes, M. I.; Daw, M. S. Embedded-atom-method functions for the fcc metals Cu, Ag, Au, Ni, Pd, Pt, and their alloys. *Phys. Rev. B* 1986, *33*, 7983, Erratum: ibid, *Phys. Rev. B 37*, 10378 (1988).
(49) Adams, J. B.; Foiles, S. M.; Wolfer, W. G. Self-diffusion and impurity diffusion of fcc metals using the five-frequence model and the Embedded Atom Method. *J. Mater. Res.* **1989**, *4*, 102.
(50) Abascal, J. L. F.; Vega, C. A general purpose model for the condensed phases of water: TIP4P/2005. *J. Chem. Phys.* **2005**, *123*, 234505.
(51) Hockney, R. W.; Eastwood, J. W. *Computer simulation using particles*; CRC Press, 1988.
(52) Dou, Y.; Zhigilei, L. V.; Winograd, N.; Garrison, B. J. Explosive boiling of water films adjacent to heated surfaces: A microscopic description. *J. Phys. Chem. A* **2001**, *105*, 2748−2755.
(53) Ju, S.-P. A molecular dynamics simulation of the adsorption of water molecules surrounding an Au nanoparticle. *J. Chem. Phys.* **2005**, *122*, No. 094718.
(54) Binns, C.; Prieto, P.; Baker, S.; Howes, P.; Dondi, R.; Burley, G.; Lari, L.; Kröger, R.; Pratt, A.; Aktas, S.; et al. Preparation of hydrosol suspensions of elemental and core− shell nanoparticles by co-deposition with water vapour from the gas-phase in ultra-high vacuum conditions. *J. Nanopart. Res.* **2012**, *14*, 1136.
(55) Ziegler, J. F.; Biersack, J. P.; Littmark, U. *The Stopping and Range of Ions in Matter* ; Pergamon: New York, 1985.
(56) Kresse, G.; Hafner, J. Ab initio molecular dynamics for liquid metals. *Phys. Rev. B* **1993**, *47*, 558.
(57) Kresse, G.; Furthmüller, J. Efficiency of ab-initio total energy calculations for metals and semiconductors using a plane-wave basis set. *Comput. Mater. Sci.* **1996**, *6*, 15−50.
(58) Blochl, P. E. Projector augmented-wave method. *Phys. Rev. B* **1994**, *50*, 17953−17979.
(59) Perdew, J. P.; Burke, K.; Ernzerhof, M. Generalized Gradient Approximation Made Simple. *Phys. Rev. Lett.* **1996**, *77*, 3865−3868.
(60) Grimme, S.; Antony, J.; Ehrlich, S.; Krieg, H. A consistent and accurate ab initio parametrization of density functional dispersion correction (DFT-D) for the 94 elements H-Pu. *J. Chem. Phys.* **2010**, *132*, 154104.
(61) Johnson, E. R.; Keinan, S.; Mori-Sánchez, P.; Contreras-García, J.; Cohen, A. J.; Yang, W. Revealing Noncovalent Interactions. *J. Am. Chem. Soc.* **2010**, *132*, 6498−6506.
(62) Contreras-García, J.; Johnson, E. R.; Keinan, S.; Chaudret, R.; Piquemal, J.-P.; Beratan, D. N.; Yang, W. NCIPLOT: A Program for Plotting Noncovalent Interaction Regions. *J. Chem. Theory Comput.* **2011**, *7*, 625−632.
(63) Humphrey, W.; Dalke, A.; Schulten, K. VMD−Visual Molecular Dynamics. *J. Mol. Graphics* **1996**, *14*, 33−38.
(64) Stone, J. *An Efficient Library for Parallel Ray Tracing and Animation*. M.Sc. thesis, Computer Science Department, University of Missouri-Rolla, 1998.
(65) Grimme, S.; Bannwarth, C.; Shushkov, P. A Robust and Accurate Tight-Binding Quantum Chemical Method for Structures, Vibrational Frequencies, and Noncovalent Interactions of Large Molecular Systems Parametrized for All spd-Block Elements (Z = 1-86). *J. Chem. Theory Comput.* **2017**, *13*, 1989−2009.
(66) O'Grady, K.; Bradbury, A. Particle size analysis in ferrofluids. *J. Magn. Magn. Mater.* **1983**, *39*, 91.
(67) Mayoral, A.; Barron, H.; Estrada-Salas, R.; Vazquez-Duran, A.; José-Yacamán, M. Nanoparticle stability from the nano to the meso interval. *Nanoscale* **2010**, *2*, 335−342.
(68) Wells, D. M.; Rossi, G.; Ferrando, R.; Palmer, R. E. Metastability of the atomic structures of size-selected gold nanoparticles. *Nanoscale* **2015**, *7*, 6498−6503.
(69) Rahm, J. M.; Erhart, P. Beyond magic numbers: atomic scale equilibrium nanoparticle shapes for any size. *Nano Lett.* **2017**, *17*, 5775−5781.
(70) Foster, D. M.; Ferrando, R.; Palmer, R. E. Experimental determination of the energy difference between competing isomers of deposited, size-selected gold nanoclusters. *Nat. Commun.* **2018**, *9*, 1−6.
(71) Marom, S.; Plesser, M.; Modi, R.; Manini, N.; Di Vece, M. 'Planetary' silver nanoparticles originating from a magnetron sputter plasma. *J. Phys. D: Appl. Phys.* **2019**, *52*, No. 095301.
(72) Nagata, T.; Mafuné, F. Thermal analysis of hydrated gold cluster cations in the gas phase. *J. Phys. Chem. C* **2017**, *121*, 16291−16299.
(73) Press, W. H.; Teukolsky, S. A.; Vetterling, W. T.; Flannery, B. P. *Numerical Recipes in C; The Art of Scientific Computing*, 2nd ed.; Cambridge University Press: New York, 1995.
(74) Wang, X.; Kruis, F. E.; McMurry, P. H. Aerodynamic focusing of nanoparticles: I. Guidelines for designing aerodynamic lenses for nanoparticles. *Aerosol Sci. Technol.* **2005**, *39*, 611−623.

https://dx.doi.org/10.1021/acs.jpcc.0c07346
J. Phys. Chem. C 2020, 124, 24441−24450